This is an open access article published under a Creative Commons Attribution (CC-BY) License, which permits unrestricted use, distribution and reproduction in any medium, provided the author and source are cited.

ACS AUTHORCHOICE

analytical chemistry

pubs.acs.org/ac

Article

Machine-Vision-Enabled Salt Dissolution Analysis

Jernej Štukelj,* Mikael Agopov, Jouko Yliruusi, Clare J. Strachan, and Sami Svanbäck

Cite This: *Anal. Chem.* 2020, 92, 9730−9738

Read Online

ACCESS | Metrics & More | Article Recommendations | Supporting Information

ABSTRACT: Salt formation is a well-established method to increase the solubility of ionizable drug candidates. However, possible conversion of salt to its original form of free acid or base—disproportionation—can have a drastic effect on the solubility and consequently the bioavailability of a drug. Therefore, during the salt selection process, the salt dissolution behavior should be well understood. Improved understanding could be achieved by a method that enables simultaneous screening of small sample amounts and detailed dissolution process analysis. Here, we use a machine-vision-based single-particle analysis (SPA) method to successfully determine the pH-solubility profile, intrinsic solubility, common-ion effect, pK_a, pH_{max}, and K_{sp} values of three model compounds in a fast and low sample consumption (<1 mg) manner. Moreover, the SPA method enables, with a particle-scale resolution, in situ observation of the disproportionation process and its immediate effect on the morphology and solubility of dissolving species. In this study, a potentially higher energy thermodynamic solid-state form of diclofenac free acid and an intriguing conversion to liquid verapamil free base were observed upon disproportionation of the respective salts. As such, the SPA method offers a low sample consumption platform for fast yet elaborate characterization of the salt dissolution behavior.

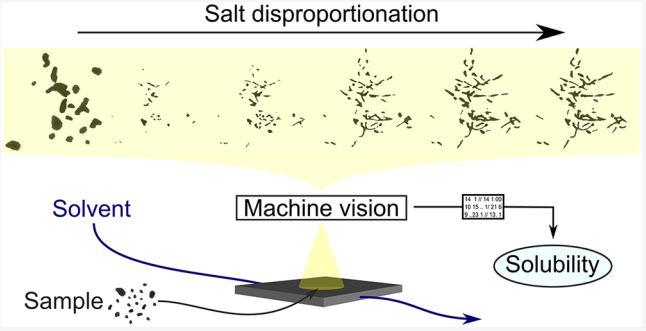

Downloaded via UNIV OF HELSINKI on November 12, 2020 at 14:40:35 (UTC).
See https://pubs.acs.org/sharingguidelines for options on how to legitimately share published articles.

Salt formation is a well-established strategy used to increase the solubility of acidic and basic drugs.[1] The initial interest in salts dates back to studies on the dissolution rates of diverse salt forms by Nelson in the 1950s.[2] This interest has been growing ever since, especially in recent decades, with the solubility of new chemical entities sharply decreasing due to production employing combinatorial chemistry and high-throughput screening.[3,4] Furthermore, potential salt form screening for a selected drug candidate is conducted in a high-throughput manner.[5,6] A rational continuation of the sequential process would be a high-throughput salt solubility or dissolution screen. However, such a method that would satisfy the high-throughput criteria and require only small sample amounts is currently lacking. Here, we use a novel machine-vision-based method to rapidly measure the solubility and monitor the dissolution behavior of three model salt compounds with minimal sample consumption.

The aqueous pH-solubility profile of an acidic or basic drug governs whether a compound can form suitable salt candidates as well as their resulting properties.[7] A crucial value is the pH_{max}, as it determines the solid phase in equilibrium with a solution at a certain pH. At the pH_{max}, free acid or base and the respective salt can coexist. For an acidic compound, a free acid is the solid at equilibrium below the pH_{max}, and a salt is formed if the pH is raised, using suitable counterions, above the pH_{max}.[8,9] The opposite relationship exists for basic drugs; a salt is formed below the pH_{max}, and a free base is in equilibrium with a solution above the pH_{max}.[10]

The equilibrium between the solid salt, acidic compound in solution, and concentration of counterions above pH_{max} is described by eq 1.[1,7,9] The equilibrium between the solid salt, basic compound in solution, and concentration of counterion below pH_{max} is described by eq 2

$$K_{sp} = [A^-][X^+] \quad (1)$$

$$K_{sp} = [BH^+][X^-] \quad (2)$$

where K_{sp} denotes the solubility product and $[A^-]$ and $[BH^+]$ are the concentrations of the acidic and basic compounds, salt solubility. $[X^+]$ and $[X^-]$ are the concentrations of the counterions. In the absence of excess counterions, the salt solubility remains unchanged. On the other hand, excess counterions can have a drastic impact on the solubility of the salts, especially those with low K_{sp} values, a phenomenon known as the common ion effect.[11,12]

For a salt of an acidic compound, if a solubility measurement is started at a pH below the pH_{max}, disproportionation will occur.[13] The result will be a precipitated free acid, which will eventually determine the solubility measured, as shown for

Received: March 10, 2020
Accepted: June 16, 2020
Published: June 16, 2020

© 2020 American Chemical Society

https://dx.doi.org/10.1021/acs.analchem.0c01068
Anal. Chem. 2020, 92, 9730−9738

phenytoin by Serajuddin et al.[14] The opposite scenario unfolds for the salt of a basic drug.[15] If salt disproportionation occurs under gastrointestinal conditions, the potential enhancement of the dissolution rate and bioavailability can be lost. Moreover, the disproportionation can occur as a direct conversion into a thermodynamically stable form of a respective free acid or base or as a more complex process, where multiple solid-state forms appear, as observed by Østergaard et al.[16]

Due to all of these parameters affecting the salt dissolution studies, interpretation of the results can be complex but nevertheless very important. Here, using the single-particle analysis (SPA) method,[17−20] we demonstrate a fast and minimal sample approach to study the dissolution behavior of salts. As the approach enables visual observation of the dissolution process, additional insight on the particle-level morphology changes and their immediate effect on solubility is obtained.

MATERIALS AND METHODS

Materials. Naproxen free acid (NAP), naproxen sodium (NAP−Na), and diclofenac sodium (DIC−Na) were acquired from Sigma-Aldrich (St. Louis, MO, USA). Verapamil hydrochloride (VER−HCl) was received from Orion Pharma (Espoo, Finland). Diclofenac free acid (DIC) was prepared by dissolving DIC−Na in a sufficient quantity of ultrapure water and adding an equimolar amount of HCl while stirring. After 10 min, the precipitate was filtered and recrystallized from ethyl acetate.

Shake-Flask (SF) Experiments. A protocol for a miniaturized SF experiment was adapted and modified from the work done by Bergström et al.[21] DIC, DIC−Na, NAP, and NAP−Na were, in excess of approximately 5 mg, added to either 400 or 600 μL of the selected buffer in Eppendorf tubes. Buffers with pH values of 2.0, 4.0, 6.0, and 8.0 were prepared according to the United States Pharmacopeia (USP) (Solutions/Buffer Solutions) (Table S1). For NAP, both phosphate and borate buffers were used at pH 8.0. The Eppendorf tubes were placed on a custom-made rotating platform (60 rpm) at room temperature (21.5 ± 1 °C). At 48, 72, and 96 h the rotation was stopped, pHs were measured, and samples were centrifuged at constant temperature and 21 100*g* for 15 min prior to sampling of the supernatant. The supernatants were appropriately diluted and analyzed with reverse-phase HPLC-UV. After 96 h, the solids were extracted and analyzed using XRPD. In addition, the pHs of single miniaturized SF experiments were measured after 24, 48, and 72 h for the USP buffers with initial pHs of 3.0, 5.0, 7.0, and 9.0 (Table S1).

HPLC Analysis. Drug concentration in the supernatants was determined using an Agilent High Performance Liquid Chromatography (HPLC) 1260 system (Agilent Technologies, Germany) coupled with a Phenomenex Gemini NX-C18, 3 μm, 100 × 4.6 mm column (Phenomenex, Torrace, CA). The temperature of the column was set to 30 °C. The mobile phase was 0.2% H_3PO_4:acetonitrile (40:60, v:v for DIC and 50:50, v:v for NAP) with a flow rate of 1 mL/min. The injection volume was 20 μL, and detection was performed at 276 nm for DIC and 254 nm for NAP. Standard solutions of DIC and NAP were prepared in 0.2% H_3PO_4:acetonitrile (50:50, v:v) and analyzed with HPLC-UV to construct the calibration curve. Calibration samples were prepared in triplicate with 0.1, 1, 10, 50, 100, and 250 μg/mL (R^2 > 0.999).

Differential Scanning Calorimetry (DSC). DSC measurements were conducted to determine the purity and the solid-state form of the initial samples. A DSC823e (Mettler-Toledo, Greifensee, Switzerland) equipped with a cooling system (Julabo FT 900, Seelbach, Germany) was used. Nitrogen with a flow rate of 50 mL/min was used as the purge gas.

Samples of 2−5 mg were packed into standard aluminum crucibles (40 μL) with pierced lids. The samples were equilibrated at 25 °C for 3 min and then linearly heated with a heating rate of 10 °C/min. Measurements of the five initial compounds were performed in triplicate. Thermal events were analyzed using STARe software (Mettler-Toledo, Greifensee, Switzerland).

X-ray Powder Diffraction (XRPD). To determine the solid-state form of the initial samples, XRPD diffractograms were recorded with an Aeris diffractometer (Malvern Panalytical B.V., Almelo, The Netherlands) using Cu Kα radiation (λ = 1.540598 Å) and a divergence slit of 0.76 mm. Samples were placed on a low-scatter-background holder and measured with a step size of 0.0108664° at 40 kV and 8.0 mA from 5° to 35° (2θ). Measurements were performed in triplicate with independent samples. Additional measurements using XRPD were performed for the remaining solids after the 96 h miniaturized SF experiments.

SPA Measurements. The SPA measurements were carried out as already previously described by Svanbäck et al. and Štukelj et al.[17,19,20] Briefly, the two main components of the SPA method are the flow-through setup and the analysis software. The flow-through setup enables trapping and machine-vision tracking of drug particles under steady flow−sink−conditions. The average measurement time is 5 min. The captured images are then analyzed using custom-made software, which is capable of semiautomatic particle recognition and tracking of the individual particle morphology throughout the measurement. The decrease in size, under sink conditions, according to Noyes and Whitney, is directly proportional to the equilibrium solubility of the compound. In this way, the solubility data from the images is extracted. Depending on the number of particles, the reported solubility values are an average of up to several hundred individual particles. For in-depth description and visuals, readers are directed to the three original papers cited above.

RESULTS AND DISCUSSION

Characterization of the Solid-State Forms. The results of the initial solid-state characterization of the five compounds used in this study are presented in Figure 1.

The experimental XRPD diffractograms of VER−HCl, NAP, and DIC match the predicted diffractograms from the Cambridge Structural Database (CSD), CURHOM, COYRUD, and SIKLIH, respectively. NAP−Na corresponds to the ASUBL CSD entry for the anhydrous salt form. There is no CSD entry for the anhydrous form of DIC−Na, but the obtained XRPD diffractogram coincides with the experimental diffractogram of the anhydrous salt reported by A. Llinàs et al.[22] Moreover, the anhydrous nature of the samples is confirmed by the absence of an endothermic dehydration event in all of the thermograms except for NAP−Na; the endothermic event with an onset at 55.8 ± 0.2 °C is associated with moisture in the sample (0.34 ± 0.02%, calculated based on the heat of evaporation of water 2400 J/g).[23] The onset temperatures of melting, seen in Figure 1b, are in good

https://dx.doi.org/10.1021/acs.analchem.0c01068
Anal. Chem. 2020, 92, 9730−9738

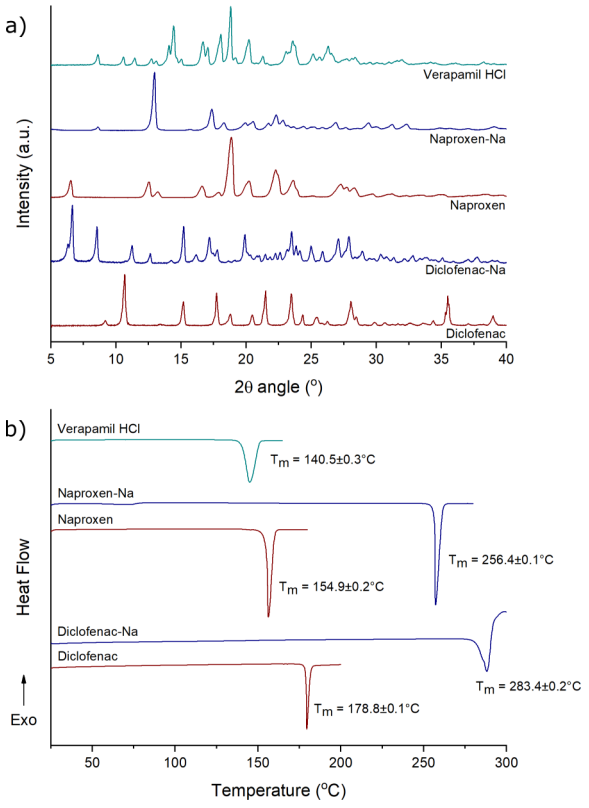

Figure 1. XRPD diffractograms (a) and DSC thermograms (b) of the studied compounds. Onsets of melting temperature are listed next to the respective melting peaks.

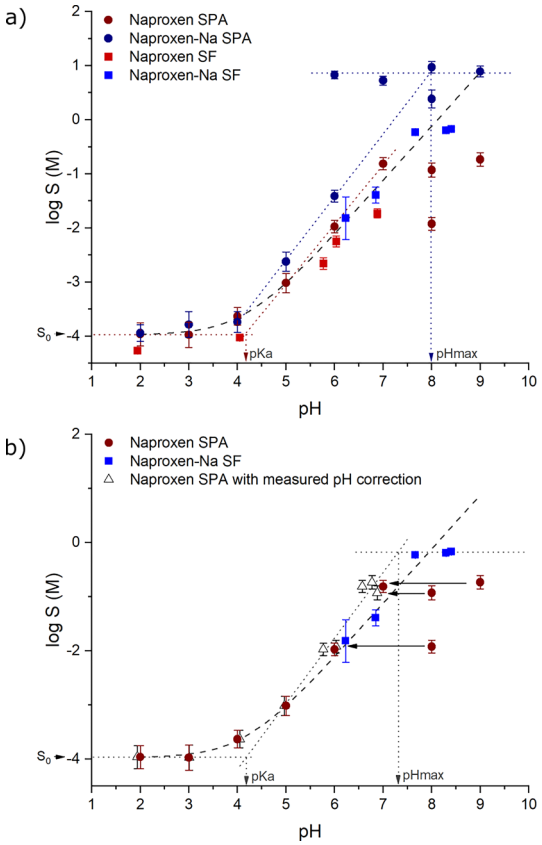

Figure 2. (a) pH-solubility profiles of NAP and NAP−Na obtained with the SPA and the SF methods. Two values for NAP−Na SPA solubility at pH 6.0 correspond to the solubilities measured before (higher) and after (lower) disproportionation. Two values for NAP SPA solubility at pH 8.0 correspond to solubilities measured in borate (lower) and phosphate (higher) USP buffer. Dashed line represents the theoretical solubility profile based on the Henderson−Hasselbalch equation. Dotted lines are fitted linearly (i) to the SPA NAP−Na solubility values to estimate the pH_{max} and (ii) to the SPA NAP solubility values to estimate the pK_a. (b) pH-solubility profile of NAP obtained with the SPA method and corrected for the surface pH change due to the self-buffering effect. Dashed line represents the theoretical solubility profile based on the Henderson−Hasselbalch equation. Dotted lines are fitted linearly to the SPA pH-corrected values to estimate the pK_a and also horizontally to the SF values of NAP−Na above pH 8 to estimate the pH_{max}. S_0 is the intrinsic solubility.

agreement with previously reported values of the thermodynamically stable forms.[24−29]

SF pH-Solubility Profile of NAP and NAP−Na. The solubility profiles of NAP and the respective sodium salt (Figure 2a) were obtained with the miniaturized SF method. Importantly, the pH of the buffers was not adjusted during the experiment. Consequently, a pH shift occurred upon dissolution of the solid material, and the data was plotted accordingly. The pH shift was most pronounced, upon addition of NAP−Na, for the buffer with an initial pH of 2.0. This can be explained by the buffer capacity originating solely from the low pH (Supporting Information S2).

When the starting material was NAP, the same form remained throughout the experiment (Figure 3). In contrast, when the starting material was NAP−Na, a solid-state change occurred. At the initial pHs of 2.0, 4.0, and 6.0, the salt converted into a free acid (Figure 3). At pH 8.0, both in borate and in phosphate buffer, the anhydrous salt converted into its hydrate form. On the basis of the solid-state landscape of NAP−Na hydrates,[30] one could assume that formation of NAP−Na tetrahydrate took place. However, XRPD diffractograms of NAP−Na at pH 8.0 (Figure 3) did not exactly match any of the diffractograms of NAP−Na hydrates (monohydrate, two dihydrate polymorphs, and tetrahydrate) reported by Raijada et al.[30] Thus, it is most likely that multiple hydrate forms were present or possibly an unreported form. Intriguingly, the samples with an initial pH of 6.0, which shifted to pH 7.7 during the experiment, and those with an initial pH of 8.0 had similar solubility values despite being in different solid-state forms at equilibrium (Figures 2a and 3). This indicates the proximity of a pH_{max}; below the pH_{max}, the solid in equilibrium is free acid, and above the pH_{max}, the solid in equilibrium is salt.

SPA pH-Solubility Profile of NAP. In Figure 2a, it can be seen that the SPA solubility values for NAP correlate well with the SF values and also with the theoretically predicted values based on the Henderson−Hasselbalch equation.[9,31] However, a deviation can be seen for the three values at pH 8 and above. The values deviate because they are plotted against the pH of the initial buffer and not against the pH on the solid−liquid interface at which dissolution actually takes place, i.e., the microenvironmental pH.[32] According to the diffusion layer theory, a layer of saturated solution surrounds a dissolving particle.[33] Therefore, one can assume that the microenvironmental pH shift in the layer of saturated solution around the particle is the same as the pH shift of the saturated solution at the end of the SF experiment. When the SPA solubility values are plotted against the pH values measured at

https://dx.doi.org/10.1021/acs.analchem.0c01068
Anal. Chem. 2020, 92, 9730−9738

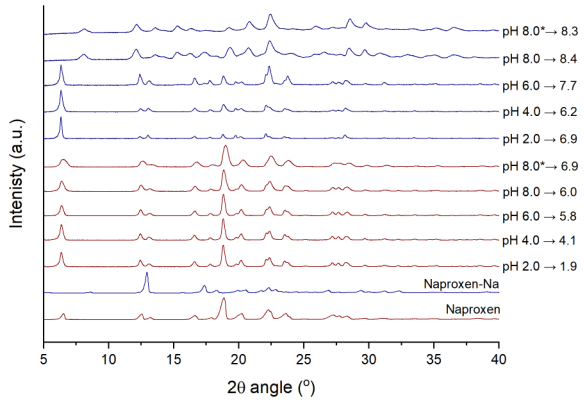

Figure 3. XRPD diffractograms of the starting materials (NAP and NAP−Na) and samples at the end of the SF experiments started with NAP (red) and NAP−Na (blue). On the right side, pH shifts that occurred during the respective SF measurement are listed. (*) Phosphate USP buffer.

the end of the respective SF experiments, a better correlation is achieved (Figure 2b). The effect of microenvironmental pH on the solubility determined with the SPA method is best seen for the two solubility values of NAP at pH 8; at this pH, borate USP buffer has a buffer capacity approximately 2-fold lower than that of phosphate USP buffer (Table S1 and Figure S1). Thus, the measured solubility in borate buffer was lower as the microenvironmental pH shift was more pronounced. However, when both solubility values are plotted against the pH at the end of the respective SF experiments, they follow the theoretically predicted pH-solubility profile. The observed pH shifts are also supported by calculations presented in the Supporting Information S2 and Table S1. Nonetheless, when estimating the pK_a values based on the two pH profiles, very similar values of 4.15 (Figure 2a) and 4.18 (Figure 2b) are obtained (Table 1). This is because the pH shift is less

Table 1. Intrinsic Solubility (S_0), pK_a, and pH_{max} Values Obtained in This Study Compared with Those in the Literature (lit.)

	naproxen	diclofenac
pK_a SPA	4.15	4.26
pK_a lit.	4.18[a]	4.08[b]
S_0 SPA (μg/mL)	25 ± 13	0.6 ± 0.3
S_0 lit. (μg/mL)	16,[a] 14[c]	1.0 ± 0.7,[a] 0.8 ± 0.2,[b] 0.9 ±0.1[d]
	naproxen sodium	diclofenac sodium
pH_{max}′ SPA	7.97	7.35
pH_{max} lit.	∼8[c]	∼8[a,e]

[a]Reference 38. [b]Reference 22. [c]Reference 9. [d]Reference 39. [e]Reference 34.

pronounced at pH values up to 7.0, which were used for estimating the pK_a in Figure 2a. For comparison, previously reported pK_a and intrinsic solubility values for NAP are listed in Table 1.

SPA pH-Solubility Profile of NAP−Na. In the SPA pH-solubility profile of NAP−Na (Figure 2a), two regions can be identified: the flat region above pH 6.0 where the actual solubility of the salt is measured and the region below pH 6.0 where, after disproportionation occurs, the solubility of NAP is measured. The process of disproportionation as observed during the SPA measurement is shown in Figure 4; at pH 3.0,

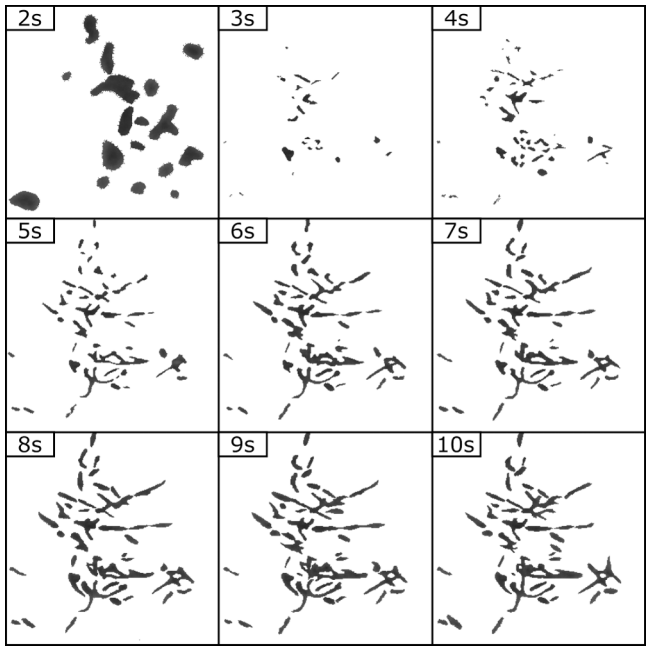

Figure 4. In situ disproportionation as observed during the SPA experiments of NAP−Na at pH 3.0. Initial dissolution followed by appearance and growth of needle-shaped particles.

instant dissolution of the initial particles is followed by the appearance of needle-shaped particles, which continue to grow for a couple of seconds and then start to dissolve. Formation of needle-shaped particles was confirmed with SEM (Supporting Information S2 and Figure S2). The solubility measured upon disproportionation of NAP−Na is in agreement with the solubility of NAP. Therefore, one can conclude that disproportionation into the thermodynamically stable solid-state form took place. However, in the study performed by Østergaard et al., formation of multiple solid-state forms upon disproportionation was observed.[16] Upon monitoring the dissolution of a compact of NAP−Na in 0.1 M HCl (pH 1.0) inside a dissolution cell with UV-imaging and Raman spectroscopy, they observed that the NAP−Na rapidly converted into three different intermediate solid-state forms followed by the slower appearance (20 min) of the thermodynamically stable NAP. It must be noted that in one of the experiments at pH 2.0 we observed a higher solubility value of 1.3 ± 0.6 mM (−2.9 in log units) upon disproportionation into smaller grain-like particles (Figure S3). However, upon multiple repetitions of the experiment, disproportionation into needle-shaped particles predominated, and therefore data from these latter experiments are plotted in Figure 2a. This behavior underscores the complex process of NAP−Na disproportionation as described by Østergaard et al.[16]

In general, the pH-solubility profile of an acidic compound is described with two curves: one where the free acid is the solid phase at equilibrium, and the second where the salt is the solid phase at equilibrium.[1] At the thermodynamic equilibrium, in certain conditions, the most stable solid-state forms of either free acid or salt (or both at pH_{max}) are present. Therefore, it is vital to consider the solid-state form of the dissolving solid when interpreting the SPA pH-solubility profile. NAP−Na disproportionated into the thermodynamically stable form of NAP in the pH range from 2 to 6. Disproportionation was also

https://dx.doi.org/10.1021/acs.analchem.0c01068
Anal. Chem. 2020, 92, 9730−9738

confirmed with FT-IR spectral analysis of the solid-state change in the SPA experiment conducted at pH 2 and 3, Supporting Information S3 and Figure S4. Moreover, the solubilities closely matched the SF and SPA values of NAP. However, for the salt region, above pH 6, such an absolute conclusion cannot be made. The SPA measurement was conducted with the anhydrous NAP−Na. This explains the 11-fold higher solubility when compared to the SF values for the in situ formed NAP−Na hydrate (Figures 2a and 3). Thus, the intersect of the two regions in Figure 2a results in an apparent pH_{max}' value of 7.97 (Table 1). On the other hand, the pH_{max} can also be determined by linearly extrapolating the pH-corrected SPA values of NAP to the SF-determined solubility of NAP−Na as shown in Figure 2b. In this case, the value of 7.30 is obtained. On the basis of the solubility of the salt above pH_{max}' measured with the SPA, an apparent solubility product of the salt K_{sp}' can be calculated using eq 1, where $[A^-]$ is the salt solubility of NAP and $[X^+]$ is the counterion (Na^+) concentration.[1] In the absence of excess counterion, $[A^-]$ equals $[X^+]$ and a K_{sp}' of 53.4 mol^2/L^2 is obtained for NAP−Na.

SF pH-Solubility Profile of DIC and DIC−Na. The solubility profiles of DIC and DIC−Na obtained with the miniaturized SF method are shown in Figure 5a. The pH of the buffers was not adjusted during the experiment. Consequently, a pH shift occurred upon dissolution of the solid material, and the data was plotted accordingly. When the starting material was DIC, it remained in the same form throughout the experiment (Figure 6). On the contrary, when the starting material was DIC−Na, a solid-state change occurred. At initial pH values of 2.0 and 4.0 the salt converted into a free acid form as shown in Figure 6. At initial pH values of 6.0 and 8.0, the anhydrous salt converted into its hydrate form. Previous studies suggest formation of DIC−Na tetrahydrate in an aqueous environment.[35,36,34,35] However, there is currently no CCD entry for the DIC−Na tetrahydrate, so the theoretical diffractogram for comparison could not be plotted. Nevertheless, the XRPD diffractogram obtained in this study (key peak positions 13.4, 17.9, 22.5, and 36.4) coincided closely with the XRPD pattern of DIC−Na tetrahydrate (DSH1) reported by M. Bartolomei et al.[36] Intriguingly, the sample with an initial pH of 2.0, which shifted to 7.9 during the experiment, had a similar solubility as the two samples with initial pH values of 6.0 and 8.0, despite being in different solid-state forms at equilibrium (Figures 5a and 6). This indicates the proximity of the pH_{max}; below the pH_{max}, the solid in equilibrium is free acid, and above the pH_{max}, the solid in equilibrium is a salt.[1]

SPA pH-Solubility Profile of DIC. The SPA solubility values for DIC correlate well with the SF values and also with the theoretically predicted values based on the Henderson−Hasselbalch equation (Figure 5a).[9,31] However, an increasing deviation from the theoretical line can be seen with the increasing pH. Similarly as with the NAP, the values deviate because they are plotted against the pH of the initial buffer and not against the pH on the liquid−solid interface at which dissolution actually takes place. If the SPA solubility values are corrected with the pH values measured at the end of the respective SF experiments, a shift to the left can be observed (Figure 5b). Observed pH shifts are also supported by calculations presented in Supporting Information S2 and Table S1. When estimating the pK_a values based on the two pH-solubility profiles, the values of 4.26 (Figure 6a) and 4.61

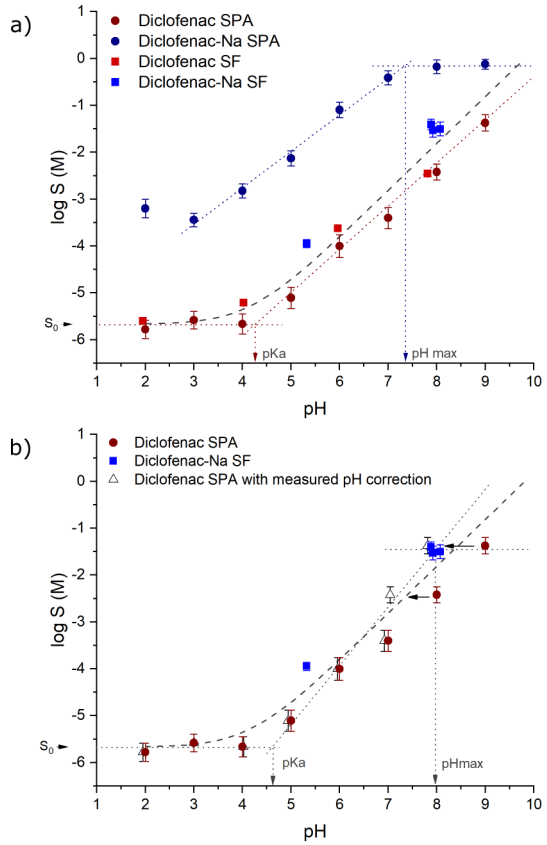

Figure 5. (a) pH-solubility profile of DIC and DIC−Na obtained with the SPA and SF methods. Dashed line represents the theoretical solubility profile based on the Henderson−Hasselbalch equation. Dotted lines are fitted linearly (i) to the SPA DIC−Na solubility values to estimate the pH_{max} and (ii) to the SPA DIC solubility values to estimate the pK_a. (b) pH-solubility profile of DIC obtained with the SPA method corrected for the surface pH change due to the self-buffering effect. Dashed line represents the theoretical solubility profile based on the Henderson−Hasselbalch equation. Dotted lines are fitted linearly to the SPA pH-corrected values to estimate the pK_a and also horizontally to the two SF values of DIC−Na that converted into hydrate form to estimate the pH_{max}. S_0 is the intrinsic solubility.

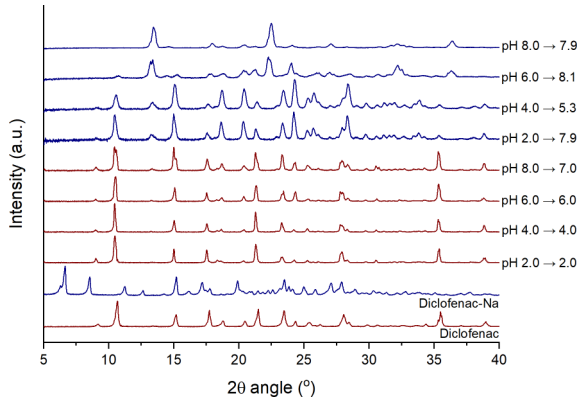

Figure 6. XRPD diffractograms of the starting material (DIC and DIC−Na). XRPD diffractograms at the end of the SF experiments started with the DIC (red) and the DIC−Na (blue). On the right, pH shifts that occurred during the respective SF measurements are listed.

(Figure 6b) were obtained. For comparison, previously reported pK_a and intrinsic solubility values for DIC are listed in Table 1.

https://dx.doi.org/10.1021/acs.analchem.0c01068
Anal. Chem. 2020, 92, 9730−9738

Despite having similar pK_a values, the microenvironmental pH shift during the dissolution of DIC was less pronounced than the microenvironmental pH shift during the dissolution of NAP. This is the consequence of the lower intrinsic solubility of DIC as described by K. Mooney et al.; the self-buffering capacity increases with increasing solubility of the unionized species of the drug.[37]

SPA pH-Solubility Profile of DIC−Na. The SPA pH-solubility profile of DIC−Na (Figure 5a) resembles the elevated pH-solubility profile of DIC. Again, two regions can be identified: the flat region roughly above pH 8 where the solubility of the salt is measured and the region below pH 8. In the region below pH 8, the disproportionation was observed during the SPA experiments up to pH 5.0 (Figure 7). For the

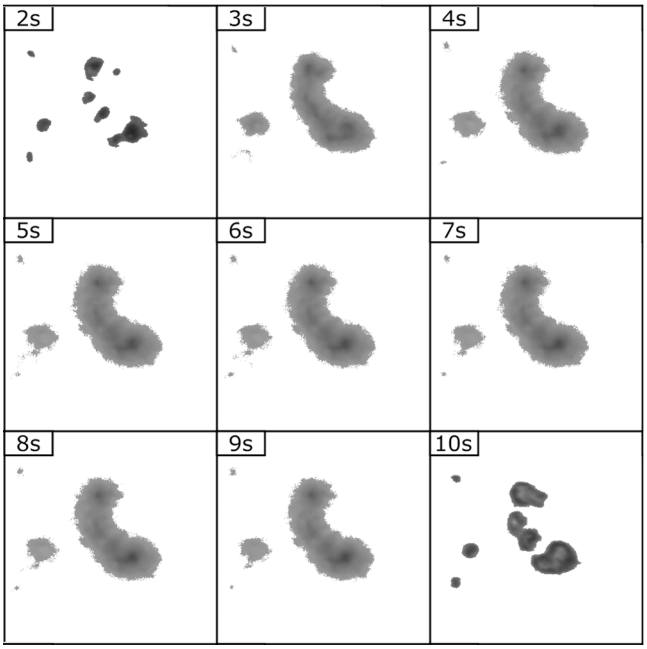

Figure 7. In situ disproportionation as observed during the SPA experiments of DIC−Na at pH 2.0. Disintegration/dissolution of initial particles resulted in formation of a supersaturated area followed by the appearance of particles with different morphology.

measurements conducted at pH 6.0 and 7.0 the disproportionation most likely also occurred as indicated by the shape of the pH-solubility profile, though it was not visually detected due to its subtle nature and the fast dissolution of particles.

Intriguingly, unlike with NAP−Na, DIC−Na exhibited higher solubility upon disproportionation when compared to the respective solubilities of DIC. Confirmation of disproportionation was achieved by measuring the FT-IR spectrum upon observation of the solid-state change in the SPA experiments conducted at pH 2 and 3, Supporting Information S3 and Figure S5. This kind of behavior for DIC−Na was, at least to our knowledge, not yet reported in the literature. Higher solubility could be the result of in situ formation of a metastable polymorph or amorphous solid of DIC. Thus, if measured for a sufficient period of time, as in a SF experiment, the solubility would decrease to that of a thermodynamically stable form of DIC.

For the salt region, as with the NAP−Na, the SPA measurement was started with anhydrous DIC−Na, which resulted in higher solubility values when compared to the respective SF values. As shown by the XRPD of the remaining SF solids in Figure 6 and based on the literature data discussed above, DIC−Na anhydrate converged during the SF experiment started at pH 6 and 8 into its tetrahydrate form.[36] There are several more hydrate forms of DIC−Na reported in the literature.[22,36,40] On the basis of these reports and on the results obtained in this study, the higher solubility of DIC−Na in the salt region measured with the SPA when compared to the SF values can be explained in two ways. The actual solubility of the anhydrous form was measured or, less likely, in the time span of the SPA experiment, the conversion to another thermodynamically unstable hydrate form occurred. Thus, as thermodynamically stable forms of free acid and hydrate salt were not measured in the SPA experiments, when starting with DIC−Na, the intersect of the two regions, Figure 5a, results in an apparent pH_{max}' value of 7.35 (Table 1). On the other hand, the actual pH_{max} can also be determined by linearly extrapolating the pH-corrected SPA values of DIC to the SF-determined solubility of DIC−Na as shown in Figure 5b. In this case, the value of 7.98 is obtained. On the basis of the solubility of the salt above pH_{max}' measured with the SPA, an apparent solubility product of the salt K_{sp}' was calculated using eq 1, and a value of 0.50 mol^2/L^2 was obtained for DIC−Na.

SPA pH-Solubility Profile of VER−HCl. A pH-solubility profile of VER−HCl as obtained with the SPA method (Figure 8) is in good agreement with the data reported by

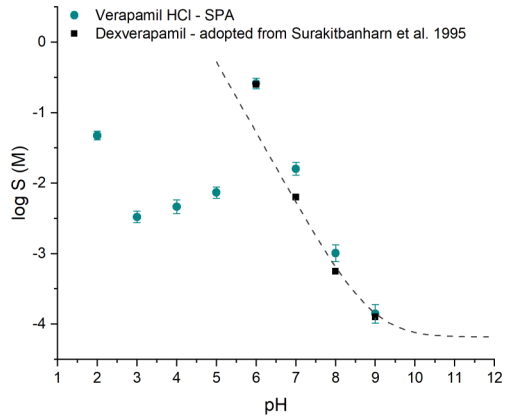

Figure 8. pH-solubility profile of VER−HCl as obtained with the SPA method and the solubility of dexverapamil as reported by Surakitbanharn et al.[41] Dashed line represents the theoretical solubility profile based on the Henderson−Hasselbalch equation, pK_a = 8.9, and $S_0 = 6.6 \times 10^{-5}$ mol/L.[41]

Surakitbanharn et al.[41] A SF experiment for VER−HCl was not conducted in this study due to the liquid solid state of verapamil free base (VER) at room temperature. This might also be the reason for the lack of solid-state characterization of the precipitate in the SF experiments conducted by Surakitbanharn et al.[41] Nevertheless, the liquid state of the VER resulted in intriguing phenomena observed during the SPA experiments.

In Figure 9a, the dissolution during the SPA experiment of VER−HCl at pH 7 can be seen. During the dissolution, the particles seem to behave as they would suddenly swell and then burst in the process. This is most likely the result of salt disproportionation forming a liquid VER. The solubility was measured before bursting of the individual particles occurred.

https://dx.doi.org/10.1021/acs.analchem.0c01068
Anal. Chem. 2020, 92, 9730−9738

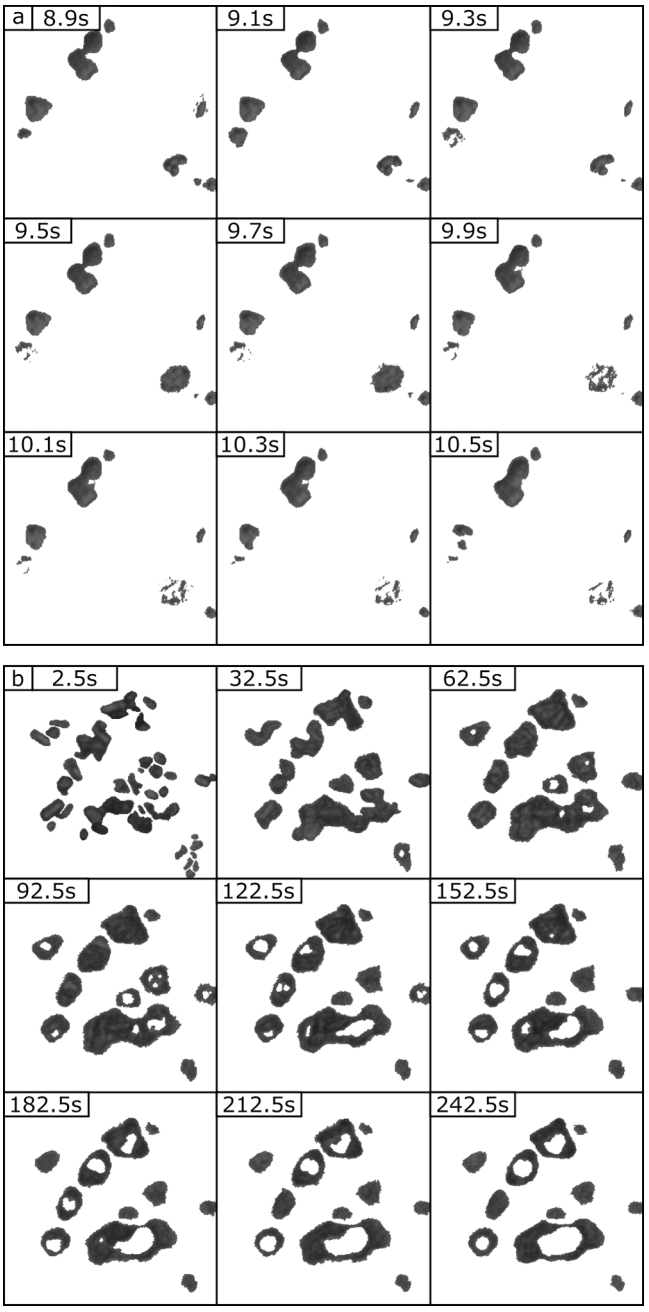

Figure 9. Change of sample morphology—in situ disproportionation—during the SPA experiments. (a) VER−HCl at pH 7.0. During dissolution, particles suddenly swell and then burst due to disproportionation into the liquid VER. (b) VER−HCl at pH 9.0. Throughout the dissolution process, particles merge into bigger rounded entities. Inside of these entities a void resembling a bubble is formed.

However, the disproportionation on the particle surface probably occurred prior to bursting, resulting in formation of a liquid free base layer surrounding the particle and hence the good agreement with the SF result obtained by Surakitbanham et al.[41]

In Figure 9b, the dissolution, during the SPA experiment, of VER−HCl at pH 9 can be seen. In this case, the particles behave differently when compared to their dissolution at pH 7. The process of solid-state change, which can be visually observed, is slower, taking several minutes compared to several seconds (Figure 9a and 9b). Particles merge forming bigger and rounder entities inside of which eventually a void, resembling a bubble, is formed. This behavior is consistent with formation of the liquid free base. Solubility values were extracted from roughly the first 50 s of the image data, before extensive changes were observed. Again, the solubility value matches that reported by Surakitbanham et al.,[41] indicating dissolution limited by the VER.

At pH 6 in Figure 8, a positive deviation from the theoretical curve can be seen. The theoretical curve was constructed based on the Henderson−Hasselbalch equation with values of pK_a = 8.9 and $S_0 = 6.6 \times 10^{-5}$ mol/L adopted from Surakitbanham et al.[41] The researchers in that study explain the positive deviation from the theoretical curve with formation of VER dimers. The fact that a positive deviation is also seen in the SPA experiments indicates the rapid formation of dimers in the unstirred layer surrounding the particles.

In the region below pH 5, no visual solid-state change was observed. Thus, one can assume the solubility of the hydrochloride salt was measured and that the pH_{max} of the respective salt is between pH 5 and pH 6. The solubility measured in this region was lower than that at pH 6 due to a substantial common-ion effect as also seen with other basic drugs.[11,42] The solubility at pH 2 was then significantly higher, which is inconsistent with the common-ion effect, but most likely occurred due to the pH-limited buffer capacity of the HCl USP buffer used at pH 2 when compared to the phthalate USP buffers used at pH 3, 4, and 5 (Supporting Information S2 and Figure S1).

CONCLUSIONS

In this study, we demonstrated the use of the SPA method for understanding the dissolution behavior of salt compounds. NAP−Na, DIC−Na, and VER−HCl were used as model salt compounds. In total, less than 1 mg of each compound was used for all of the SPA measurements. In contrast, the corresponding analyses conducted with miniaturized SF experiments require from 100 mg up to 10 g of compound, depending on the solubility. As the amount of sample needed for the SPA experiment is so small, possible total dissolution during the course of the measurement can prevent subsequent offline solid-state characterization. However, this study demonstrates that visually detectable solid-state changes may still provide crucial information for the interpretation of the measured solubility.

On the basis of the obtained pH-solubility profiles, intrinsic solubility, pK_a, pH_{max}, and K_{sp} values were determined. Moreover, a transient higher solubility of DIC−Na and intriguing behavior of VER−HCl upon disproportionation were observed. The importance of the sample solid-state and the possible microenvironmental pH shift was addressed in the context of the SPA measurements. Finally, the study has demonstrated that the SPA method is a powerful tool as it enables visual in situ observation of the salt disproportionation process on the particle level and its direct impact on the solubility of a potential salt candidate. As such, the method has much potential as a low sample consumption platform enabling elaborate characterization of the salt dissolution behavior.

https://dx.doi.org/10.1021/acs.analchem.0c01068
Anal. Chem. 2020, 92, 9730−9738

■ ASSOCIATED CONTENT

Supporting Information

The Supporting Information is available free of charge at https://pubs.acs.org/doi/10.1021/acs.analchem.0c01068.

Theoretical pH shift calculation, buffer capacity estimation, SEM image of NAP−Na after disproportionation at pH 3.0, NAP−Na disproportionation at pH 2.0 with SPA, confirmation of disproportionation of NAP−Na and DIC−Na with FT-IR (PDF)

■ AUTHOR INFORMATION

Corresponding Author

Jernej Štukelj − *Drug Research Program and Division of Pharmaceutical Chemistry and Technology, University of Helsinki, 00790 Helsinki, Finland; The Solubility Company Oy, 00790 Helsinki, Finland;* orcid.org/0000-0002-1452-4310; Email: jernej.stukelj@helsinki.fi

Authors

Mikael Agopov − *The Solubility Company Oy, 00790 Helsinki, Finland*

Jouko Yliruusi − *The Solubility Company Oy, 00790 Helsinki, Finland*

Clare J. Strachan − *Drug Research Program and Division of Pharmaceutical Chemistry and Technology, University of Helsinki, 00790 Helsinki, Finland;* orcid.org/0000-0003-3134-8918

Sami Svanbäck − *The Solubility Company Oy, 00790 Helsinki, Finland; Drug Research Program and Division of Pharmaceutical Chemistry and Technology, University of Helsinki, 00790 Helsinki, Finland*

Complete contact information is available at: https://pubs.acs.org/10.1021/acs.analchem.0c01068

Author Contributions

J.Š., J.Y., C.J.S., and S.S. conceived the project and designed the experiments. M.A helped with the data processing. J.Š. performed the experiments and wrote the manuscript. J.Y., C.J.S., and S.S. reviewed the manuscript.

Funding

J.Š. acknowledges funding from the Doctoral Programme in Drug Research (DPDR).

Notes

The authors declare the following competing financial interest(s): J.Š., M.A., J.Y., and S.S. are shareholders of The Solubility Company Oy that owns the intellectual property rights to the SPA method.

■ REFERENCES

(1) Serajuddin, A. T. M. *Adv. Drug Delivery Rev.* **2007**, *59*, 603−616.
(2) Nelson, E. *J. Am. Pharm. Assoc., Sci. Ed.* **1957**, *46* (1957), 607−614.
(3) Lipinski, C. A. *J. Pharmacol. Toxicol. Methods* **2000**, *44*, 235−249.
(4) Gardner, C. R.; Walsh, C. T.; Almarsson, Ö. *Nat. Rev. Drug Discovery* **2004**, *3*, 926−934.
(5) Kimura, K.; Onishi, S.; Moriyama, K. *J. Pharm. Sci.* **2018**, *107*, 1870−1878.
(6) Remenar, J. F.; MacPhee, J. M.; Larson, B. K.; Tyagi, V. A.; Ho, J. H.; McIlroy, D. A.; Hickey, M. B.; Shaw, P. B.; Almarsson, Ö. *Org. Process Res. Dev.* **2003**, *7*, 990−996.
(7) Stahl, P. H.; Wermuth, C. G. *Handbook of Pharmaceutical Salts: Properties, Selection, and Use*, 1st ed.; VHCA: Zürich and Wiley-VCH: Weinheim, 2002.
(8) Serajuddin, A. T. M.; Jarowski, C. I. *J. Pharm. Sci.* **1985**, *74*, 148−154.
(9) Chowhan, Z.T. *J. Pharm. Sci.* **1978**, *67*, 1257−1260.
(10) Kramer, S. F.; Flynn, G. L. *J. Pharm. Sci.* **1972**, *61*, 1896−1904.
(11) Zannou, E. A.; Ji, Q.; Joshi, Y. M.; Serajuddin, A. T. M. *Int. J. Pharm.* **2007**, *337*, 210−218.
(12) David, S. E.; Timmins, P.; Conway, B. R. *Drug Dev. Ind. Pharm.* **2012**, *38*, 93−103.
(13) Thakral, N. K.; Kelly, R. C. *Int. J. Pharm.* **2017**, *520*, 228−240.
(14) Serajuddin, A. T. M.; Jarowski, C. I. *J. Pharm. Sci.* **1993**, *82*, 306−310.
(15) Serajuddin, A. T. M.; Sheen, P. C.; Mufson, D.; Bernstein, D. F.; Augustine, M. A. *J. Pharm. Sci.* **1986**, *75*, 492−496.
(16) Østergaard, J.; Wu, J. X.; Naelapaa, K.; Boetker, J. P.; Jensen, H.; Rantanen, J. *J. Pharm. Sci.* **2014**, *103*, 1149−1156.
(17) Svanbäck, S.; Ehlers, H.; Antikainen, O.; Yliruusi, J. *Anal. Chem.* **2015**, *87*, 5041−5045.
(18) Svanbäck, S. Experimental, Results and Discussion. *Toward accurate high-throughput physicochemical profiling using image-based single-particle analysis*; University of Helsinki: Helsinki, 2016; pp 22−45.
(19) Štukelj, J.; Svanbäck, S.; Kristl, J.; Strachan, C. J.; Yliruusi, J. *Anal. Chem.* **2019**, *91*, 3997−4003.
(20) Štukelj, J.; Svanbäck, S.; Agopov, M.; Löbmann, K.; Strachan, C. J.; Rades, T.; Yliruusi, J. *Anal. Chem.* **2019**, *91*, 7411−7417.
(21) Bergström, C. A. S.; Norinder, U.; Luthman, K.; Artursson, P. *Pharm. Res.* **2002**, *19*, 182−188.
(22) Llinàs, A.; Burley, J. C.; Box, K. J.; Glen, R. C.; Goodman, J. M. *J. Med. Chem.* **2007**, *50*, 979−983.
(23) Di Martino, P.; Barthélémy, C.; Palmieri, G. F.; Martelli, S. *Eur. J. Pharm. Sci.* **2001**, *14*, 293−300.
(24) Yoshida, M. I.; Gomes, E. C. L.; Soares, C. D. V.; Cunha, A. F.; Oliveira, M. A. *Molecules* **2010**, *15*, 2439−2452.
(25) Bettinetti, G. P.; Sorrenti, M.; Rossi, S.; Ferrari, F.; Mura, P.; Faucci, M. T. *J. Pharm. Biomed. Anal.* **2002**, *30*, 1173−1179.
(26) Kim, Y. S.; Rousseau, R. W. *Cryst. Growth Des.* **2004**, *4*, 1211−1216.
(27) Giordano, F.; Rossi, A.; Pasquali, I.; Bettini, R.; Frigo, E.; Gazzaniga, A.; Sangalli, M. E.; Mileo, V.; Catinella, S. *J. Therm. Anal. Calorim.* **2003**, *73*, 509−518.
(28) Žilnik, L. F.; Jazbinšek, A.; Hvala, A.; Vrečer, F.; Klamt, A. *Fluid Phase Equilib.* **2007**, *261*, 140−145.
(29) Palomo, M. E.; Ballesteros, M. P.; Frutos, P. *J. Pharm. Biomed. Anal.* **1999**, *21*, 83−94.
(30) Raijada, D.; Bond, A. D.; Larsen, F. H.; Cornett, C.; Qu, H.; Rantanen, J. *Pharm. Res.* **2013**, *30*, 280−289.
(31) Po, H. N.; Senozan, N. M. *J. Chem. Educ.* **2001**, *78*, 1499−1503.
(32) Østergaard, J.; Jensen, H.; Larsen, S. W.; Larsen, C.; Lenke, J. *J. Pharm. Biomed. Anal.* **2014**, *100*, 290−293.
(33) Higuchi, W. I. *J. Pharm. Sci.* **1967**, *56*, 315−324.
(34) Fini, A.; Garuti, M.; Fazio, G.; Alvarez-Fuentes, J.; Holgado, M. A. *J. Pharm. Sci.* **2001**, *90*, 2049−2057.
(35) Ledwidge, M. T.; Corrigan, O. I. *Int. J. Pharm.* **1998**, *174*, 187−200.
(36) Bartolomei, M.; Bertocchi, P.; Antoniella, E.; Rodomonte, A. *J. Pharm. Biomed. Anal.* **2006**, *40*, 1105−1113.
(37) Mooney, K. G.; Mintun, M. A.; Himmelstein, K. J.; Stella, V. J. *J. Pharm. Sci.* **1981**, *70*, 13−22.
(38) Avdeef, A.; Berger, C. M.; Brownell, C. *Pharm. Res.* **2000**, *17*, 85−89.
(39) Stuart, M.; Box, K. *Anal. Chem.* **2005**, *77*, 983−990.
(40) Muangsin, N.; Prajaubsook, M.; Chaichit, N.; Siritaedmukul, K.; Hannongbua, S. *Anal. Sci.* **2002**, *18*, 967−968.
(41) Surakitbanharn, Y.; McCandless, R.; Krzyzaniak, J. F.; Dannenfelser, R. M.; Yalkowsky, S. H. *J. Pharm. Sci.* **1995**, *84*, 720−723.

(42) Joshi, H. N.; Tejwani, R. W.; Davidovich, M.; Sahasrabudhe, V. P.; Jemal, M.; Bathala, M. S.; Varia, S. A.; Serajuddin, A. T. M. *Int. J. Pharm.* **2004**, *269*, 251−258.

https://dx.doi.org/10.1021/acs.analchem.0c01068
Anal. Chem. 2020, 92, 9730−9738